
Performance Characteristics Obtained for a New 3-Dimensional Lutetium Oxyorthosilicate–Based Whole-Body PET/CT Scanner with the National Electrical Manufacturers Association NU 2-2001 Standard

Marco Brambilla, MS¹; Chiara Secco, MS¹; Marco Dominietto, MS¹; Roberta Matheoud, MS¹; Gianmauro Sacchetti, MD²; and Eugenio Inglese, MD²

¹Health Physics Department, Azienda Ospedaliera Maggiore della Carità, Novara, Italy; and ²Nuclear Medicine Department, Azienda Ospedaliera Maggiore della Carità, Novara, Italy

This article reports the results of performance measurements obtained for the lutetium oxyorthosilicate (LSO)–based whole-body PET/CT scanner Biograph 16 HI-REZ with the National Electrical Manufacturers Association (NEMA) NU 2-2001 standard. The Biograph 16 HI-REZ combines a multislice (16-slice) spiral CT scanner with a PET scanner composed of 24,336 LSO crystals arranged in 39 rings. The crystal dimensions are $4.0 \times 4.0 \times 20$ mm³, and the crystals are organized in 13×13 blocks coupled to 4 photomultiplier tubes each. The 39 rings allow the acquisition of 81 images 2.0 mm thick, covering an axial field of view of 162 mm. The low- and high-energy thresholds are set to 425 and 650 keV, respectively, acquiring data within a 4.5-ns-wide coincidence window. **Methods:** Performance measurements for the LSO-based PET/CT scanner were obtained with the NEMA NU 2-2001 standard, taking into account issues deriving from the presence of intrinsic radiation. **Results:** The results obtained with the NEMA NU 2-2001 standard measurements were as follows: average transverse and axial spatial resolutions (full width at half maximum) at 1 cm and at 10 cm off axis of 4.61 (5.10) mm and 5.34 (5.91) mm, respectively; average sensitivity of 4.92 counts per second per kilobecquerel for the 2 radial positions (0 and 10 cm); 34.1% system scatter fraction; and peak noise equivalent count (NEC) rates of 84.77 kilocounts per second (kcps) at 28.73 kBq/mL ($k = 1$ in the NEC formula; noiseless random correction) and 58.71 kcps at 21.62 kBq/mL ($k = 2$; noisy random correction). **Conclusion:** The new integrated PET/CT system Biograph 16 HI-REZ has good overall performance, with, in particular, a high resolution, a low scatter fraction, and a very good NEC response.

Key Words: instrumentation; quality assurance; NEMA standard; PET/CT; Biograph 16 HI-REZ

J Nucl Med 2005; 46:2083–2091

Received May 10, 2005; revision accepted Aug. 8, 2005.
For correspondence or reprints contact: Marco Brambilla, MS, Servizio di Fisica Sanitaria, A.O. Maggiore della Carità, C.so Mazzini 18-28100, Novara, Italy.

E-mail: marco.brambilla@maggioreosp.novara.it

The NU 2-2001 (hereafter referred to as N-01) standard published by the National Electrical Manufacturers Association (NEMA) (1) is widely used to characterize PET scanner performance (2–5). A recent publication by Watson et al. (6) indicated that performance tests of lutetium oxyorthosilicate (LSO)–based PET scanners cannot be conducted strictly according to the N-01 standard because of the presence of intrinsic radioactivity within the LSO crystals, giving rise to intrinsic random and true coincidences. Some changes to the N-01 specifications were suggested, mainly affecting the estimation of sensitivity, scatter, randoms, and count losses. A key concept of the recommendations, introduced to properly take into account the events resulting from the intrinsic activity, is the use of an activity concentration threshold (a_{ref}) above which the response of the system is determined more by the radiation originating external to the detectors than by the intrinsic decay.

The background single-event counting rate resulting from intrinsic activity depends on the detector assembly and the energy discrimination settings. In the specific case of the LSO block detector used in the Biograph 16 HI-REZ scanner (Siemens Medical Solutions) (hereafter referred to as the B-HIREZ scanner), the background single-event counting rate is typically about 5.9 kilocounts per second (kcps) per block (850 kcps for the whole detection system) when a 425- to 650-keV acceptance energy window is used. As a consequence, when the ratio of randoms to trues (RTR) is plotted against the activity concentration in an N-01 counting-rate test, a minimum value of 0.11 is encountered at $2 \times s_{int} = 11.8$ kcps (s_{int} is the block intrinsic single-event rate); this value corresponds to a measured a_{ref} of 0.69 kBq/mL in the 70-cm-long N-01 scatter phantom (total activity, 15.2 MBq), as shown in Figure 1. In the absence of intrinsic activity, the RTR ratio would have fallen monotonically to

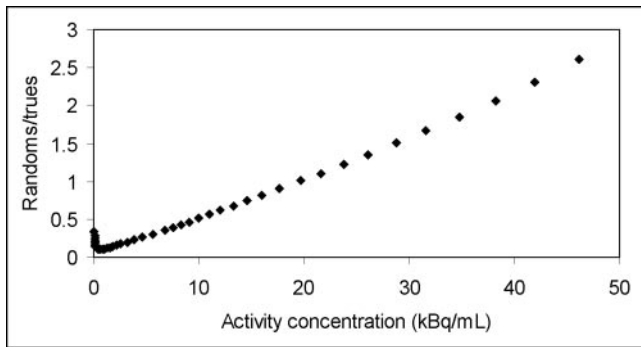


FIGURE 1. RTR ratio for N-01 counting-rate test performed on B-HIREZ scanner as function of effective average activity concentration.

zero as the activity diminished; Figure 1 shows an increase at low activity levels because of the progressive predominance of the LSO background over the activity placed in the scanner field of view (FOV). In addition to random coincidences, the intrinsic radiation also may give rise to a small number of true coincidences. The total rate of such events is only about 5 counts per second (cps) when no objects are placed in the scanner FOV and decreases to 1.5 cps when the 70-cm-long N-01 scatter phantom is placed in the FOV without any activity in the relative insert. Thus, the effect of intrinsic trues is not significant and does not need to be compensated for when the scanner sensitivity and scatter fraction (SF) are measured with very low activity levels in the relative phantoms.

The PET performance characteristics of the B-HIREZ scanner were determined by use of the N-01 standard with the modification suggested by Watson et al. (6) to take into account intrinsic radioactivity in the estimation of the SF, counting-rate characteristics, and accuracies of corrections for count losses and randoms.

MATERIALS AND METHODS

B-HIREZ Scanner

The LSO-based whole-body PET/CT B-HIREZ scanner combines a 16-slice helical CT scanner (Somatom Sensation 16; Siemens Medical Solutions) with a high-resolution PET scanner (HI-REZ) coupled to new, highly improved detection electronics (PICO-3D). The PET component of the tomograph has no septa, thus allowing 3-dimensional (3D)-only acquisitions. The detector ring is made of 144 detection units (blocks) containing 169 single crystals ($4 \times 4 \times 20$ mm³ each) arranged in a 13×13 array and coupled to 4 photomultiplier tubes. In this configuration, 24,336 crystals cover a 162-mm axial FOV with 39 rings generating 81 image planes 2 mm thick for each acquired bed. The low- and high-energy threshold are set to 425 and 650 keV, respectively. The coincidence time window is set to 4.5 ns, taking full advantage of the short decay time and high light output of LSO by means of the PICO-3D electronic circuit which, in addition to the extremely narrow coincidence window, has a very short coincidence time resolution (500 ps) and a 15% overall system energy resolution.

The CT portion of the B-HIREZ scanner can acquire images having slice thicknesses ranging from 0.6 to 10 mm. The minimum rotation time is 0.5 s/360°. The tube current can be varied between 28 and 500 mA, and the tube voltage can be set to 80, 100, 120, and 140 kilovolts (peak). The table feed per 360° rotation of the x-ray tube can be changed from 1 to 20 mm, with a maximum allowed spiral scan time of 100 s.

The main technical characteristics of this new integrated PET/CT system are summarized in Tables 1 and 2 for CT and PET, respectively.

Test Phantom Sets

The N-01 tests require 3 sets of phantoms. The first phantom set is the International Electrotechnical Commission body phantom set, which consists of a torso cavity, a removable lung insert, and 6 spheres that can be filled; the spheres have an inner diameter (ID) of 10–37 mm. The second phantom set is the scatter phantom set, including a solid circular polyethylene cylinder with a specific

TABLE 1
Main CT Technical Characteristics of B-HIREZ Scanner

Characteristic	Value
Scan mode	Helical, axial, scout
Aperture (cm)	70
Transverse scan field (cm)	50
Maximum no. of CT slices	16
Nominal slice width (mm)	0.6, 0.75, 1, 1.5, 2, 3, 4, 5, 6, 7, 8, 10
Tube voltage (kV)	80, 100, 120, 140
Tube current (mA)	28–500
Detector material	Solid state (ultrafast ceramic [Siemens Medical Solutions])
No. of elements along z-axis	24
No. of detectors/row	672
Total effective length of detector array (mm)	24
Rotation time (s)/360° rotation	0.42, 0.5, 0.75, 1.0, 1.5
Pitch factor (volume pitch)	0.5–2.0 (1–20)
Spiral scan time (s)	100
Helical interpolation algorithm available	Adaptive multiplane reconstruction
Heat capacity (heat units $\times 10^6$)	5.3
Maximum power (kW)	60

TABLE 2

Main PET Technical Characteristics of B-HIREZ Scanner

Characteristic	Value
Detector ring diameter (cm)	83.0
Detector material	LSO
No. of individual crystals	24,336
No. of crystals/ring	624
No. of detector rings	39
No. of image planes/bed	81
Crystal size (mm ³)	4 × 4 × 20
Face of crystal block (mm ²)	52 × 2
Crystal array/block	13 × 13
No. of detector blocks	144
Patient port diameter (cm)	70
Axial FOV (cm)	16.2
Transaxial FOV (cm)	58.5
Axial sampling interval (mm)	2.0
Coincidence window (ns)	4.5
Energy window (keV)	425–650

gravity of 0.96, an outside diameter (OD) of 203 mm, an overall length of 700 mm, and an 800-cm-long plastic tube that can be filled; the tube has a 3.2-mm ID and is inserted in a hole drilled parallel to the central axis of the cylinder at a 45-mm radial distance. The third phantom set is the sensitivity phantom set, consisting of 5 concentric aluminum tubes (each 70 cm long) and a 1.8-mL polyethylene tube that is inserted into the central sleeve and that can be filled. These NEMA phantoms are manufactured by Data Spectrum Corp. and are marketed by Biodex Medical Systems. Detailed information and specifications for the N-01 phantoms can be found at www.biodex.com. As specified by the N-01 standard, all measurements were performed with the ¹⁸F isotope.

Spatial Resolution

Source Preparation and Acquisition Protocol. The N-01 standard specifies that the activity should be placed for an axial extent of less than 1 mm in a glass capillary tube with an ID of <1 mm. It is further required that the source be placed parallel to the tomograph long axis for all measurements. As pointed out by Erdi et al. (2), positron annihilation is not confined to the location of ¹⁸F in the fluid; positrons may stream up the capillary and annihilate in the glass of the tube. This positron range effect may tend to elongate the imaged source in the direction of the tube; indeed, Erdi et al. measured a significantly wider axial resolution when the source was placed along the axial direction than when it was placed transaxially in the scanner, demonstrating that the source was asymmetric. Consequently, we used the method suggested by Bailey et al. (7) for the point source fabrication; we used commercially available molecular sieves (Zeolites; Molecular Sieve 13X, 8/12 beads 100g, part 05268 [Alltech Associates]) for adsorption of radioactivity onto small (2-mm-diameter) beads. Soaking the beads in an ¹⁸F-FDG solution of ~0.5 GBq/mL for 1–2 min, we produced sources containing 2.5–3 MBq each. The total activity placed in the FOV was thus <10 MBq for each acquisition. Under these conditions, as demonstrated by Watson et al. (6), the N-01 criterion that both dead time and the ratio of random events to total events be <5% was fulfilled. The point sources were placed on a piece of tape, which was suspended by means of a needle. By use of a source holder, the 3 point sources were positioned in the scanner FOV as follows: $x = 0$ cm, $y = 1$ cm; $x = 0$ cm, $y = 10$

cm; and $x = 10$ cm, $y = 0$ cm. Once in place, the 3 point sources were aligned (axially) in the scanner FOV by use of laser lights. Two sets of emission measurements were obtained with the sources centered at 2 axial positions in the scanner FOV: in the center and at one quarter of the axial FOV (4.05 cm). For each position, more than 2×10^6 counts were acquired to ensure adequate statistics.

Reconstruction and Data Analysis. Data were corrected for scanner geometry, crystal efficiency, random coincidences (by use of the delayed coincidence window technique), and system dead time. For each position, the images were reconstructed by use of the filtered backprojection (FBP) algorithm onto a 336×336 matrix with a ramp filter. The reconstruction zoom was set to 2. The pixel size was 1 mm. Transverse spatial resolution was calculated for each point source position as full width at half maximum (FWHM) and full width at 10th maximum (FWTM) of the resulting point-spread function by interpolating the adjacent pixels on the radial and tangential profiles. An axial profile was derived from the number of counts in each slice versus the slice number, and axial resolution was measured as the FWHM and FWTM of such a profile. Radial and tangential resolutions (FWHM and FWTM) for each radial position (1 and 10 cm) were averaged for both of the axial positions.

Sensitivity

Source Preparation and Acquisition Protocol. A polyethylene tube (ID, 1 mm; OD, 3 mm; length, 70 mm) was filled with a total of 2.14 MBq and placed in the center of 5 concentric aluminum sleeves (IDs, 3.9, 7.0, 10.2, 13.4, and 16.6 mm). The prepared phantom was suspended in the center of the transaxial FOV and oriented parallel to the scanner long axis. To compensate for counting-rate losses as the source decayed, the measurements were started with all of the aluminum tubes in the phantom. After each acquisition (240 s each), the most external tube was removed, and the acquisition was repeated. The same measurements were repeated at a 10-cm radial offset from the center of the transaxial FOV.

Data Analysis. Raw-data sinograms were used for sensitivity analysis. Single-slice rebinning was applied to the sinograms to assign counts in the oblique line of responses to the image slices where the line of responses crosses the scanner axis. The total system sensitivity at each radial position was calculated by dividing the total counting rate in the absence of any attenuating material (R_0) by the corresponding activity. R_0 was determined by fitting the natural logarithm of measured counting rates, after correction for activity decay, as a function of the sleeve thickness. Linear regression was used to fit the data, obtaining an extrapolated value for R_0 . The sensitivity for each plane was calculated according to the N-01 standard.

Scatter Fraction and Noise Equivalent Count (NEC) Rates

Source Preparation and Acquisition Protocol. The phantom used was the 20-cm-diameter solid polyethylene cylinder with an overall length of 70 cm and a line source threaded along its length, parallel to its central axis, at 4.5 cm from its center. The phantom was centered both in the transverse FOV and in the axial FOV so that the line source was at the position nearest the patient table. The line source was filled with 1,047.47 MBq of ¹⁸F initial activity, enough to achieve counting rates beyond the peak trues and NEC rates. Forty-six frames were acquired: the first 10 with a 10-min duration, with a 5-min gap between the scans, during which the phantom was extracted from the FOV, the second 10 with a 15-min

duration, and the last 26 with a 20-min duration, with a 10-min gap between the scans. Data were acquired over 18 h, and for each acquisition, more than 2.5×10^6 coincidence counts were stored. Separate prompt and delayed sinograms were acquired by use of the standard delayed coincidence window technique.

Data Analysis. 3D sinograms were rebinned by use of the single-slice rebinning algorithm. Data analysis was carried out by the modified procedure suggested by Watson et al. (6). Instead of estimating the randoms ($R_{randoms}$) from the prompt sinograms by correcting the totals (R_{TOT}) for trues (R_{trues}) and scatter ($R_{scatter}$), these values were computed directly from the delayed window sinogram with the same bins as those used for the prompt sinogram analysis. The scatter event rate for each slice (i) at each activity (j) was computed as follows:

$$R_{scatter,i,j} = R_{TOT,i,j} - R_{trues,i,j} - R_{randoms,i,j}$$

neglecting the contribution of intrinsic trues. The SF was estimated as follows:

$$SF_{i,j} = \frac{R_{s,i,j}}{R_{trues,i,j} + R_{scatter,i,j}}$$

NEC rates were calculated as follows:

$$NEC \text{ rate} = \frac{R_{trues}^2}{R_{trues} + R_{scatter} + kR_{randoms}}$$

Two NEC rate curves were generated, for $k = 1$ (noiseless random correction) and $k = 2$ (noisy random correction).

Accuracies of Corrections for Count Losses and Randoms

Source Preparation and Acquisition Protocol. The same phantom as that used for the SF and NEC rate tests was used. The line source was filled with 635 MBq of ^{18}F initial activity, enough to achieve counting rates beyond the peak NEC rates ($k = 2$). Twenty-six frames were acquired: the first 11 with a 15-min duration, the intermediate 11 with a 20-min duration, followed by a 40-min gap between the scans, and the last 4 with a 20-min duration. Data were acquired over 14.75 h, and for each acquisition, more than 2.5×10^6 coincidence counts were stored.

Reconstruction and Data Analysis. All counting-rate-dependent corrections (dead-time losses and random coincidences) were applied. Data were reconstructed by use of the Fourier rebinning-ordered-subset expectation maximization (OSEM) iterative reconstruction, with 2 iterations and 8 subsets. A 4-mm FWHM gaussian filter was applied to the image after reconstruction along the axial and transaxial directions. The data were reconstructed over a 128×128 matrix with a 2-mm pixel size and slice thickness.

Once reconstructed, the images were analyzed by drawing a circular region of interest (ROI) (18-cm diameter) centered on the reconstructed images of the phantom. The counting-rate error ($\% \Delta R$) as a function of the effective activity concentration was calculated as the deviation of the true counting rate (R) from a linear trend extrapolated from the low-activity acquisitions (6), at which dead-time losses were negligible (R_{extrap}), as follows:

$$\% \Delta R = 100 \left(\frac{R}{R_{extrap}} - 1 \right)$$

Image Quality and Attenuation and Scatter Correction Accuracies

Source Preparation and Acquisition Protocol. Image quality was evaluated by imaging a torso phantom containing 6 coaxial

isocentered spheres with IDs of 10, 13, 17, 22, 28, and 37 mm. A 5-cm-diameter cylindrical insert filled with foam pellets with an average density of 0.30 g/mL was positioned in the center of the phantom to simulate lung tissue. The phantom was filled with a solution of water and ^{18}F (5.4 kBq/mL) and the 4 smallest spheres with a radioactivity concentration 7.9 times that of the background (lesion-to-background activity ratio [L/B] = 8). The remaining 2 spheres (28- and 37-mm IDs) were filled with nonradioactive water. In a second acquisition, the radioactivity concentration in the hot sphere was 3.9 times that of the background (L/B = 4). Once filled, the phantom was positioned centrally in the scanner FOV (both axially and transaxially). To simulate the body activity from outside the scanner FOV, the 70-cm scatter phantom was positioned at the edge of the torso phantom. The plastic tube inside the scatter phantom was filled with 119.2 and 112.2 MBq of ^{18}F for the 2 acquisitions. The imaging time was set to simulate a total body scan (100-cm total axial imaging distance in 60 min, according to the N-01 standard). Because the transmission scan is performed with the CT scanner, the contribution of its relative scan time to the total imaging time can be considered negligible. Data acquisition time was determined by considering the 12.2-cm (16.2- to 4-cm overlap) axial distance between consecutive bed positions in a total-body scan to be 7.32 min. We used 0.32 min for the positioning and CT scans and 7 min for the PET emission scan.

Reconstruction and Data Analysis. Data were corrected for random coincidences, normalization, dead-time losses, scatter, and attenuation. The results are reported for 3 different reconstructions: 1 FBP reconstruction (all-pass filter) and 2 attenuation-weighted OSEM iterative reconstructions, with 2 iterations and 8 subsets and with 4 iterations and 14 subsets. In all cases, Fourier rebinning was used to reduce the 3D dataset to a 2-dimensional-equivalent one, and a 4-mm FWHM gaussian filter was applied to the image after reconstruction along the axial and transaxial directions. The data were reconstructed over a 128×128 matrix with a 5.25-mm pixel size and a 2-mm slice thickness.

To evaluate the hot- and cold-sphere contrast, circular ROIs with diameters equal to the physical IDs of the spheres were drawn over PET images. Twelve background ROIs (37-mm diameter) were drawn on the central slice as well as on slices at ± 10 mm and ± 20 mm axially. Smaller ROIs (10, 13, 17, and 28 mm) were drawn concentric to the 37-mm background ROIs. In addition, a 5-cm ROI was drawn (in each phantom slice) on the central lung insert to assess the accuracies of the attenuation and scatter corrections. To minimize the influence of the operator in the ROI positioning, an automatic routine was developed with IDL 6.1 (Research Systems, Inc.); the operator needed only to establish the center of the 13-mm sphere and of the lung insert in the central slice. Positioning and determination of dimensions of the remaining ROIs on spheres, the background, and the lung insert were done automatically and closely following N-01 recommendations. ROI analysis was performed by taking into account partial pixels as well.

The hot-sphere contrast recovery coefficient (Q_H) was calculated as follows:

$$Q_H = \frac{(C_{hot}/C_{bkgd}) - 1}{(a_{hot}/a_{bkgd}) - 1}$$

where C_{hot} and C_{bkgd} are the averages of the counts measured in the hot-sphere ROI and of the counts measured in all background

TABLE 3
3D Performance Characteristics of NEMA N-01 Standard

Parameter	Position	FWHM/FWTM	Direction	Value
Spatial resolution (mm)	1 cm	FWHM	Radial and tangential	4.61
		FWTM		8.76
	10 cm	FWHM	Radial	5.34
			Tangential	5.34
		FWTM	Radial	10.05
		Tangential	10.87	
Axial resolution (mm)	1 cm	FWHM		5.10
		FWTM		9.27
	10 cm	FWHM		5.93
		FWTM		10.91
Sensitivity (cps/kBq)	0 cm			4.87
	10 cm			4.97
Scatter fraction (%)				34.1
Counting rate (kcps; kBq/mL)				
Peak trues rate				274.19; 31.59
Peak NEC rate ($k = 1$)				84.77; 28.73
Peak NEC rate ($k = 2$)				58.71; 21.62

ROIs, respectively, and a_{hot}/a_{bkgd} is the ratio of activities in the hot sphere and in the background.

The cold-sphere contrast recovery coefficient (Q_C) was calculated as follows:

$$Q_C = 1 - (C_{cold}/C_{bkgd}),$$

where C_{cold} is the average of the counts measured in the cold-sphere ROI.

The accuracies of the attenuation and scatter corrections were calculated as the residual errors in the lung region as follows:

$$\Delta C_{lung} = 100(C_{lung}/C_{bkgd}),$$

where C_{lung} is the average counts in the lung ROI. The variation coefficients of the means (N_j) in the background ROIs for the various sphere sizes were taken as a measure of background variability, as follows:

$$N_j = 100(SD_j/C_{bkgd,j}),$$

where SD_j is the SD of the background ROI counts for sphere j .

To assess the effect of image noise level on contrast measurement, repeated scans over a range of activity levels for $L/B = 8$ and $L/B = 4$ activity ratios were performed. The measured activity levels were 1.7, 1, and 0.59 times the standard background activity level. For this study, only FBP reconstruction was used. The percent variation coefficients of the contrast values across the range of activity levels were computed.

RESULTS

Spatial Resolution

Transverse spatial resolution and axial resolution are reported in Table 3. For the point spread at $x = 0$ cm, $y = 1$ cm, radial and tangential resolutions were averaged. Also, spatial resolution values for the point spread at $x = 0$ cm, $y = 10$ cm and $x = 10$ cm, $y = 0$ cm were averaged. Both axial and transaxial FWHM values degraded by about 0.8 mm when moving from 1 to 10 cm away from the central axis of the scanner. Spatial resolution was isotropic at a

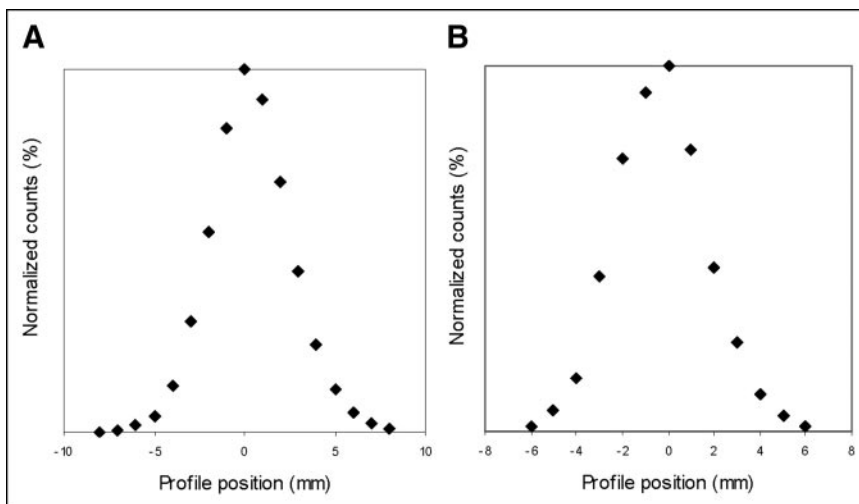


FIGURE 2. Spatial resolution for point source at 1 cm off center. (A) Axial profile. (B) Transverse profile.

radial distance of 10 cm from the center of the FOV. In Figure 2, the axial and transverse profiles for the 1-cm off-center source are shown as representative examples of the spatial response of the PET system.

Sensitivity

The sensitivity test results are shown in Table 3. The total sensitivity values for radial positions of 0 and 10 cm were 4.87 and 4.97 kcps/MBq, respectively. No intrinsic trues correction was applied, as discussed previously. The axial sensitivity profiles of the system for the on-axis and 10-cm-off-axis positions are shown in Figure 3.

Scatter Fraction and Counting Rates

Figure 4 shows the results of the scatter fraction and counting-rate test. Activity concentration is effective average activity concentration. NECR = NEC rates.

Figure 4 shows the results of the scatter fraction and the counting-rate test. Table 3 shows the values for the scatter fraction and the counting rate of the system and the corresponding effective average activity concentrations for the peak NEC rates for $k = 1$ and $k = 2$. Intrinsic scatter fraction measured at low activity levels was 34.1%. Scatter fraction increased slightly as activity increased. The system scatter fraction corresponding to the peak NEC rate (21.62 kBq/mL for $k = 2$) was 36.2%. The measured peak NEC rate for $k = 1$ was 84.77 kcps at 28.73 kBq/mL, and the peak NEC rate for $k = 2$ was 58.71 kcps at 21.62 kBq/mL.

Accuracies of Corrections for Count Losses and Randoms

Figure 5 shows the relative counting-rate errors as percentages for the highest, lowest, and average values for the slices versus the effective average activity concentrations. Data corrections were not designed to work above the saturation point of the scanner; therefore, we reported values only over the meaningful range, which was ~28 kBq/mL or less. Over the clinical range of the scanner (activity at peak NEC rate for $k = 2$ and below), the maximum bias was less than 12% and the average bias was less than 4%.

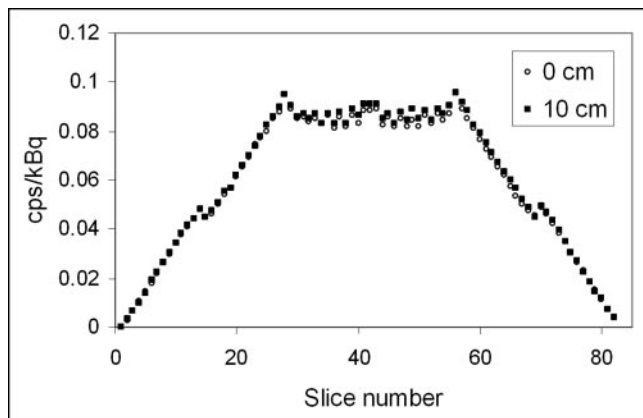


FIGURE 3. Axial sensitivity profile at center of FOV and at 10 cm off center.

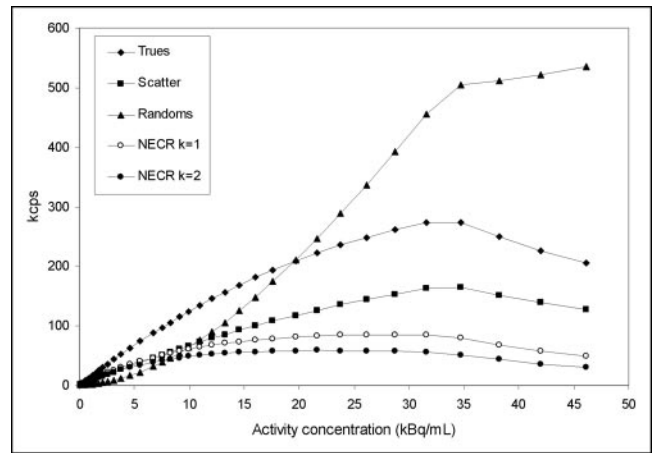


FIGURE 4. Scatter fraction and counting-rate test. Activity concentration is effective average activity concentration. NECR = NEC rates.

Image Quality and Attenuation and Scatter Correction

In Tables 4 and 5, the results obtained are shown in terms of hot-sphere recovery coefficient, cold-sphere contrast, average residual attenuation and scatter correction errors in the lung region, and background variability for $L/B = 4$ and $L/B = 8$, respectively. The results of the repeat measurements for hot-sphere contrast indicated that these values were reproducible within 0.7%–1.5% for $L/B = 8$ and 2.7%–5.6% for $L/B = 4$. For cold spheres, values were reproducible within 2.6%–5.6% in the 2 experiments. No systematic trend for contrast versus activity was observed. Figure 6 shows the transverse image slices through the plane of the spheres for both L/B activity ratios and for each of the 3 considered reconstructions (negative values in the FBP-reconstructed images were set to 0).

DISCUSSION

The new integrated PET/CT system B-HIREZ is a fully 3D tomograph designed for cardiology, neurology, and oncology PET for diagnostic, research, and radiotherapy studies (the 70-cm scanner patient port allows positioning of

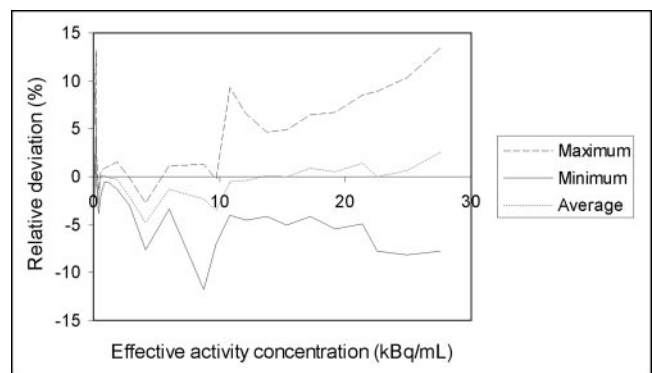


FIGURE 5. Percent maximum, minimum, and average values of relative counting-rate error over each slice for each acquisition.

TABLE 4
Percent Contrast, Background Variability, and Average Lung Residual for L/B = 4

Sphere size (mm)	Contrast (%)			Background variability (%)		
	2i × 8s*	4i × 14s†	FBP (relative deviation)	2i × 8s*	4i × 14s†	FBP
10	22	48	46 (4.4)	2.8	6.6	8.1
13	32	51	48 (4.1)	2.3	5.8	5.7
17	54	68	65 (5.6)	2.0	5.0	4.2
22	65	74	72 (2.7)	1.9	4.1	3.3
28	51	68	73 (2.6)	1.8	3.3	2.2
37	54	73	73 (4.7)	2.1	3.4	1.8
Average residual (%) over lung insert	34	17	22			

*Two iterations and 8 subsets.
†Four iterations and 14 subsets.

radiotherapy patients by means of a dedicated flat pallet). The detector geometry, which permits very small LSO crystal elements to be assembled and efficiently bonded to the PET/CT scanner design, and the PICO-3D technology are the key points of the B-HIREZ scanner. The new, very fast electronics allow an overall improvement in scanner performance in terms of scatter and randoms rejection, and noise-equivalent (and total) counting rates increase at all activity levels; these data are particularly evident at the high doses (about 925–1,110 MBq) typically used for short-lived radiotracer studies, optimizing the final results of the studies. Furthermore, the very good spatial resolution of the B-HIREZ system strongly reduced the partial-volume effect, improving the tracer uptake estimation and the contrast for all of the lesions (particularly the smallest ones).

The aim of this work was the physical characterization of the PET performance of the B-HIREZ scanner according to the N-01 standard and the modifications introduced to take into account the presence of LSO intrinsic radioactivity (6). The results of the physical characterization are discussed below, parameter by parameter, and compared with the performance of a widely used LSO-based PET scanner, the Biograph LSO Duo scanner, produced by Siemens Medical Solutions; the latter scanner has a similar architecture but a

smaller number of (larger) crystals, arranged in a different geometry and coupled to coincidence electronics different from those used in the B-HIREZ scanner.

Intrinsic Activity

The background single-event counting rate resulting from intrinsic activity depends on the details of detector construction and energy discrimination settings. Erdi et al. (2) reported for the LSO block detector and electronics used in the Biograph LSO Duo PET/CT scanner an intrinsic singles rate on the order of 1,000 kcps in the whole scanner for a 350- to 650-keV acceptance energy window, which corresponds to a block singles rate (s_{int}) of about 7.5 kcps. For the B-HIREZ scanner, this value was 850 kcps in the whole scanner for a 425- to 650-keV acceptance energy window, which corresponds to a block singles rate (s_{int}) of about 5.9 kcps. Moreover, they measured an intrinsic true coincidence rate of about 600 cps with no objects in the FOV of the scanner, whereas the corresponding value in the B-HIREZ scanner was only 5 cps. Because of this negligible value, no corrections for intrinsic trues were applied in the sensitivity and SF calculations. A key concept in the recommendations provided to properly take into account the LSO intrinsic activity is the characteristic extrinsic activity (or activity

TABLE 5
Percent Contrast, Background Variability, and Average Lung Residual for L/B = 8

Sphere size (mm)	Contrast (%)			Background variability (%)		
	2i × 8s*	4i × 14s†	FBP (relative deviation)	2i × 8s*	4i × 14s†	FBP
10	30	52	46 (1.0)	2.7	4.3	5.5
13	45	60	55 (1.4)	2.4	3.4	3.5
17	63	73	68 (1.5)	2.2	3.2	2.4
22	72	77	74 (0.7)	2.1	3.3	2.0
28	51	66	69 (5.4)	2.1	3.6	1.9
37	52	70	72 (5.6)	2.0	3.5	1.6
Average residual (%) over lung insert	34	16	16			

*Two iterations and 8 subsets.
†Four iterations and 14 subsets.

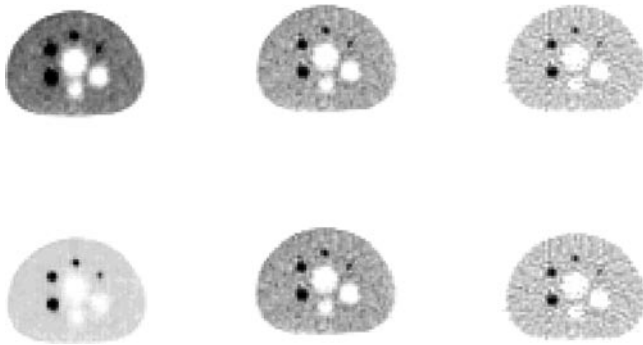


FIGURE 6. Central-slice images for image quality measurements. (Top row) 4:1 contrast ratio. (Bottom row) 8:1 contrast ratio. For each contrast, reconstructions with FBP, OSEM with 2 iterations and 8 subsets, and OSEM with 4 iterations and 14 subsets (from right to left) are shown.

concentration, when appropriate) threshold $a_{\text{ref}} = 2s_{\text{int}}$, above which the response of the system is determined more by the radiation originating external to the detectors than by the internal activity. In the N-01 standard counting-rate test, Erdi et al. measured an a_{ref} of 0.61 kBq/mL in the 70-cm-long scatter phantom (total activity, 13.4 MBq). The corresponding values in the B-HIREZ scanner were 0.69 kBq/mL and 15.2 MBq. These differences originate from the reduced acceptance energy window in the B-HIREZ scanner, which diminishes intrinsic singles and trues as well as system sensitivity. Thus, notwithstanding the lower s_{int} values seen with the B-HIREZ scanner, the values for a_{ref} are higher.

Spatial Resolution

Spatial resolution was measured as the FWHM and FWTM of a point-spread function with molecular sieves; because of their small size (less than half of the system resolution) and relatively high uptake, they were shown to be excellent tools for spatial resolution measurements. Transaxial and axial resolutions were 4.6 and 5.3 mm, respectively, at 1 cm off center. In comparison with those of the Biograph LSO Duo scanner (transverse resolution, 6.3 mm; axial resolution, 6.8 mm) (2), the crystal dimensions and plane spacing of the B-HIREZ scanner allowed significant improvements in both the transverse resolution and the axial sampling. Degradation of axial and transaxial FWHM resolution when moving from 1 to 10 cm away from the central axis of the scanner was limited to 0.8 mm; the corresponding value measured by Erdi et al. was 1 mm (2).

Sensitivity

The lower sensitivity of the B-HIREZ scanner than of the Biograph LSO Duo scanner (4.9 kcps/MBq vs. 6.1 kcps/MBq) was partly attributable to the higher low-energy threshold of the discrimination energy window (425 keV vs. 350 keV) and partly attributable to the reduced volume of the LSO crystals (7,787 cm³ vs. 9,000 cm³).

Scatter Fraction

The scatter fraction was significantly lower with the B-HIREZ scanner (34.1%) than with the Biograph LSO Duo scanner (47%) as a result of the higher low-energy threshold of the acquisition energy window (425 keV vs. 350 keV).

Counting-Rate Performance

In general, the B-HIREZ system showed very good counting-rate performance. This finding was proved by a comparison with the performance of the Biograph LSO Duo scanner (e.g., N-01 standard NEC rate peak: 58.99 kcps at 21.68 kBq/mL vs. 31.4 kcps at 12.6 kBq/mL). The introduction of the ultrafast PICO-3D electronic circuit allowed the coincidence window to be reduced to 4.5 ns; that of the Biograph LSO Duo scanner is 6 ns. Such a short coincidence time window allows random rate reduction by about a factor of 1.3 relative to the Biograph LSO Duo scanner. The B-HIREZ scanner showed a peak trues rate of 274.2 kcps at an activity concentration of 31.59 kBq/mL, demonstrating an improvement over the Biograph LSO Duo scanner, which achieved a peak trues rate of 171 kcps at 21 kBq/mL (2). Moreover, it should be considered that activity levels beyond 30 kBq/mL generally are not clinically relevant in whole-body FDG studies because of limitations on patient radiation exposure.

Scatter and Attenuation Correction Accuracies

In the N-01 standard test, scatter and attenuation correction accuracies were evaluated for a low-density (polystyrene) cold activity region simulating the human lungs. The scatter and attenuation correction errors depended on the reconstruction algorithm used and, in the case of an iterative algorithm, on the number of iterations and subsets. The residual errors were 34% and 17% for attenuation-weighted OSEM (8 subsets and 2 iterations and 14 subsets and 4 iterations, respectively) and 22% for FBP. These values are similar to those reported by Erdi et al. (32% and 13%), with the exception of FBP, for which a value of 0 was observed (2).

Image Quality

Placement of the spheres, lungs, and background ROIs on the transaxial slices of the phantoms was performed automatically with IDL 6.1 software. This process speeds up the image quality analysis (which otherwise would be very time-consuming) and maximizes intra- and interobserver reproducibilities. The results presented in Tables 4 and 5 are based on the assayed values for the L/B activity ratios (3.9 and 7.9). The uncertainties in these ratios imply corresponding uncertainties in the resulting hot-sphere contrast on the order of $\pm 10\%$. The results for OSEM with 4 iterations and 14 subsets were similar to those for FBP, both in contrast recovery and in background variability. OSEM with 2 iterations and 8 subsets yielded considerably smoother images with corresponding reduced contrast and background variability, as already pointed out by Erdi et al. (2).

In comparison with the Biograph LSO Duo scanner, the B-HIREZ scanner showed improved contrast for hot and cold lesions, for both L/B activity ratios, and for each reconstruction algorithm used. The background variabilities were similar. The contrast improvement usually exceeded the 10% threshold derived from uncertainties attributable to phantom-filling procedures and may be ascribed to the improved spatial resolution and counting-rate characteristics of the B-HIREZ scanner.

CONCLUSION

With an LSO-based scanner, it is not possible to exactly follow the N-01 standard because of the presence of intrinsic radioactivity. With the B-HIREZ scanner, some modifications of the procedures are needed only for the scatter fraction and counting-rate test, whereas the sensitivity test can be done in accordance with the N-01 standard.

The new fully integrated B-HIREZ scanner shows good overall performance as a result of optimized crystal geometry and a fast electronic circuit, which significantly improved spatial resolution, diminished the scatter fraction,

and increased the peak NEC rate relative to the previous dedicated LSO-based PET and PET/CT scanners produced by the same manufacturer.

REFERENCES

1. National Electrical Manufacturers Association. *NEMA Standards Publication NU-2-2001: Performance Measurements of Positron Emission Tomographs*. Rosslyn, VA: National Electrical Manufacturers Association; 2001.
2. Erdi YE, Nehmeh SA, Mulnix T, Humm JL, Watson CC. PET performance measurements for an LSO-based combined PET/CT scanner using the National Electrical Manufacturers Association NU 2-2001 standard. *J Nucl Med*. 2004;45:813–821.
3. Bettinardi V, Danna M, Savi A, et al. Performance evaluation of the new whole-body PET/CT scanner: Discovery ST. *Eur J Nucl Med Mol Imaging*. 2004;31:867–881.
4. Surti S, Karp JS. Imaging characteristics of a 3-dimensional GSO whole-body PET camera. *J Nucl Med*. 2004;45:1040–1049.
5. Mawlawi O, Podoloff DA, Kohlmyer S, et al. Performance characteristics of a newly developed PET/CT scanner using NEMA standards in 2D and 3D modes. *J Nucl Med*. 2004;45:1734–1742.
6. Watson CC, Casey ME, Eriksson L, Mulnix T, Adams D, Bendriem B. NEMA NU 2 performance tests for scanners with intrinsic radioactivity. *J Nucl Med*. 2004;45:822–826.
7. Bailey DL, Snowdon G, Cooper RG, Roach PJ. The use of molecular sieves to produce point sources of radioactivity. *Phys Med Biol*. 2004;49:N21–N29.

